Green Chemistry

PAPER

View Article Online
View Journal | View Issue

Cite this: *Green Chem.*, 2025, **27**, 5851

Enhancing the electroreduction of N_2 and/or O_2 on MoS_2 using a nanoparticulate intrinsically microporous polymer (PIM-1)†

Caio V. S. Almeida,[a,b] Lara K. Ribeiro,[a,b] Lucia H. Mascaro,*[a] Mariolino Carta,[c] Neil B. McKeown[d] and Frank Marken*[b]

Received 4th February 2025,
Accepted 23rd April 2025

DOI: 10.1039/d5gc00612k

rsc.li/greenchem

The electrochemical nitrogen reduction reaction under ambient/mild conditions offers a low-carbon alternative to the Haber–Bosch process for synthesizing NH_3, especially when coupled to solar electricity and employed on site without shippping. However, low selectivity and the competing electrocatalytic hydrogen formation presently limit practical applications. In this report, we enhance the performance of the MoS_2 electrocatalyst (a 2D material with electroactive sites for N_2 fixation) by interface engineering using a polymer of intrinsic microporosity (PIM-1) in nanoparticulate form. We report an improved selectivity and activity for both O_2 reduction to H_2O_2 and N_2 reduction to NH_3 (confirmed by $^{15}N_2$ isotope experiments). With the addition of PIM-1 nanoparticles, the NH_3 yield rate is 61.2 μg h^{-1} mg^{-1} (employing 0.6 mg cm^{-2} MoS_2), almost twice as high as that for MoS_2 without PIM-1. The faradaic efficiency reaches 45.4% at −0.85 V *vs.* Ag/AgCl in 0.1 M phosphate buffer at pH 7. Experiments with direct air feed (approx. 21% O_2 and 78% N_2) demonstrate successful ammonia production even in the presence of ambient oxygen.

Green foundation

1. This study addresses the production of ammonia by electroreduction of nitrogen from air. Green processes must avoid fossil energy and raw materials. We go one step further by avoiding separation of oxygen and nitrogen to almost mimic biological processes in nitroplasts. At the same time, we introduce fundamentally new chemistry based on microporous polymer enhanced triphasic reactions.
2. Qualitatively, we achieve ammonia production from air with solar energy as a big step towards green fertilizer production. For quantitative aspects, we would have to scale up and get more realistic yields (more engineering). We hope to do this in the future.
3. This work requires more depth in terms of exploring other catalysts and reasons for nitrogen over oxygen reduction. Ultimately, then we have to make a device to demonstrate the technology on a farm.

Introduction

Ammonia (NH_3), as a precursor of fertilisers and nitrogenous chemicals, plays a critical role in agricultural and industrial development.[1,2] NH_3 has 17.6 wt% hydrogen and is considered an emerging easily transported carrier of hydrogen compatible with renewable energy sources such as solar and wind power.[3] Growing concerns over energy and environmental issues provide incentives to explore new sustainable low-carbon technologies (competing with the Haber–Bosch process[4]) to produce NH_3. This could lead to a more decentralized production to replace the conventional industrial process that requires a high consumption of fossil fuels with emissions of CO_2 (currently almost 3% of global emissions).[3–5] A new process would be desirable avoiding separation of gases and using direct air feed.

There are prominent biological processes for ambient nitrogen fixation, for example based on nitroplasts[6,7] or on enzyme catalysis.[8,9] Photochemical catalyst systems are under development[10,11] to harvest energy from sunlight coupling nitrogen fixation to quencher oxidation.[12] Photocatalytic nitrogen fixation processes have been suggested even in open air.[13]

The electrochemical nitrogen reduction reaction could be a promising alternative approach due to the possibility of produ-

[a]*Department of Chemistry, Federal University of São Carlos, São Carlos, SP, 13565-905, Brazil. E-mail: lmascaro@ufscar.br*
[b]*Department of Chemistry, University of Bath, Claverton Down, Bath BA2 7AY, UK. E-mail: f.marken@bath.ac.uk*
[c]*Department of Chemistry, Faculty of Science and Engineering, Swansea University, Grove Building, Singleton Park, Swansea, SA2 8PP, UK*
[d]*EaStCHEM, School of Chemistry, University of Edinburgh, Joseph Black Building, David Brewster Road, Edinburgh, Scotland EH9 3JF, UK*
† Electronic supplementary information (ESI) available. See DOI: https://doi.org/10.1039/d5gc00612k

cing NH_3 without a quencher and under mild conditions, such as ambient temperature and ambient atmospheric pressure[14] (essentially replacing both hydrogen production and thermal activation in the Haber–Bosch process with overpotential activation in a single electrocatalytic process). The strong and non-polar N≡N bond (bond energy 941 kJ mol^{-1}) makes N_2 adsorption and activation difficult. The competitive hydrogen evolution reaction lowers nitrogen reduction selectivity and poses a major challenge in the design of suitable nitrogen reduction electrocatalysts.[15] It is shown here that not only the catalyst, but also the catalyst environment can contribute to process efficiency.

Transition metal dichalcogenide materials have been intensively investigated as nitrogen reduction electrocatalysts due to their electronic properties such as availability of occupied and empty d-orbitals.[16,17] The empty d-orbitals of transition metal dichalcogenides accept electrons from the lone-pair electrons of N_2 molecules. The electrons in the occupied d-orbitals can be back-donated to the adsorbed N_2 molecule thus activating the N≡N bond.[18,19] MoS_2 has unique characteristics, such as large specific surface area and abundant surface/edge atoms due to its two-dimensional defective structure.[20,21] Mo and S are present in natural nitrogenase enzymes, responsible for ambient N_2 fixation in biological systems.[15,22] These features make MoS_2 a promising catalyst for nitrogen reduction.[23–25] In a recent study, Almeida *et al.*[22] synthesized amorphous MoS_2 electrocatalyst, which exhibited high nitrogen reduction activity with a faradaic efficiency of 35.4% at −0.2 V *vs.* RHE (at pH 7, corresponding to −0.81 V *vs.* Ag/AgCl). With addition of iron oxide, MoS_2 was shown to produce ammonia with 54.9% faradaic efficiency at −0.2 V *vs.* RHE.[22] Here, rather than optimizing the catalyst chemistry, the effects of a gas-storing microporous polymer deposit on local gas activity and on catalyst performance are investigated. An increase in local nitrogen gas activity is proposed to enhance catalysis.

Polymers of intrinsic microporosity (PIMs) are based on molecularly rigid materials composed of contorted ladder-like structures[26,27] and have been introduced to electrochemistry recently in liquid phase systems such as in oxygen reduction and hydrogen evolution and for formic acid oxidation.[28,29] Beneficial features of PIMs include ease of processing from solution, a molecularly rigid structure creating a high surface area, and porosity with pores typically 1 nm in size.[26] The N_2 reduction can benefit from the triphasic electrocatalytic interface formed by the deposition of PIM-1 nanoparticles.[28] O_2 and H_2 gas storage effects in aqueous media have been reported.[28,30] N_2 gas is expected to be stored in a similar manner inside the porous PIM-1 structure (Fig. 1; similar to oxygen gas storage under very similar conditions[30]) close to the electrode surface, locally increasing N_2 activity/availability and preventing the formation of bubbles at the catalyst surface, which would block active catalyst sites.[31]

We enhance the nitrogen reduction performance for the MoS_2 electrocatalyst by assembling PIM-1 nanoparticle aggregates of typically 100 nm diameter as a film on the electrode surface. The PIM-1 nanoparticles deposit improves the activity and selectivity of MoS_2 not by changing the catalyst, but by changing the environment at the interface. Aqueous phosphate buffer (pH 7; sodium based) is employed to minimise pH gradient effects. This results in an NH_3 yield rate of 61.2 μg h^{-1} mg^{-1}, almost twice higher than that determined for bare MoS_x and with a faradaic efficiency as high as 45.4% at −0.85 V *vs.* Ag/AgCl in 0.1 M phosphate buffer solution. Yield rate and faradaic efficiency are high and comparable to recent literature reports.[18] The results suggest that N_2 can be accumulated/stored in PIM-1 nanoparticles to give an enhanced activity at the electrode surface in a triphasic reaction environment to facilitate nitrogen reduction.

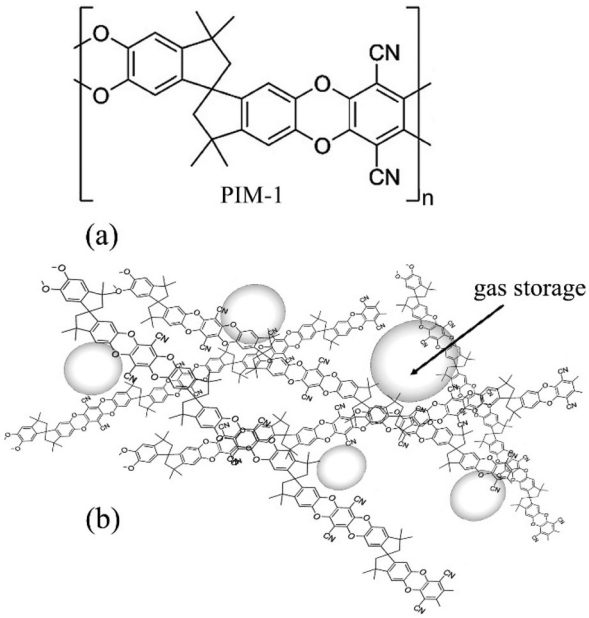

Fig. 1 (a) Molecular structure of PIM-1 and (b) illustration of gas storage (hypothetical) within the hydrophobic microporous structure.

Results and discussion

Formation and characterization of MoS_2 electrocatalyst film

Fig. 2 shows the voltammetric profile for 50 cycles of MoS_2 electrodeposition onto carbon paper (Toray, area 0.25 cm^2 front and 0.25 cm^2 back; total geometric area 0.5 cm^2; thickness 0.28 mm). In the first cycle the currents are small, however with the increasing of depositing cycles it was possible to observe a better definition of the anodic (A) and cathodic (C) processes, which are observed at −0.30 V and −0.79 V *vs.* Ag/AgCl, respectively. The total charge of the peaks increases as a function of the number of deposition cycles, indicating a continuous deposition of MoS_2 onto the carbon paper.[32]

According to the mechanism of MoS_x formation reported by Tan *et al.*,[33] the cathodic peak C may be associated with the reduction of the $[MoS_4]^{-2}$ ions to MoS_2 (eqn (1)).

$$[MoS_4]^{2-} + 2H_2O + 2e^- \rightarrow MoS_2 + 2HS^- + 2OH^- \quad (1)$$

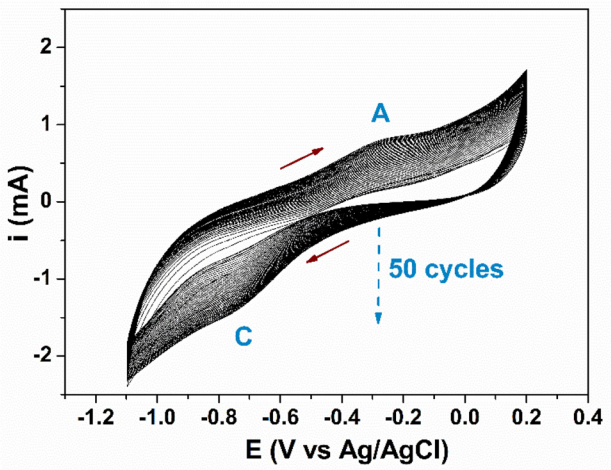

Fig. 2 Cyclic voltammograms for 50 cycles of MoS_2 electrodeposition in a solution containing 5.0 mmol L^{-1} $(NH_4)_2MoS_4$ in 0.1 mol L^{-1} $NaClO_4$ on carbon paper (0.5 cm^2) with a scan rate of 50 mV s^{-1}.

During the anodic sweep, MoS_2 oxidation can occur in the presence of HS^- adsorbed on the surface, generating MoS_3 (peak A and reaction (2)). When the scan direction is reversed, an additional reaction occurs. $[MoS_4]^{2-}$ may react with active sites provided by MoS_3 for the formation of MoS_2 (reaction (3)). The processes described by reaction (2) and (3) continue repeatedly as the number of cycles increases.

$$MoS_2 + 2HS^- \rightarrow MoS_3 + H_2S + 2e^- \quad (2)$$

$$MoS_3 + [MoS_4]^{2-} + 3H_2O + 4e^- \rightarrow 2MoS_2 + 3HS^- + 3OH^- \quad (3)$$

Fig. 3 shows typical SEM images at different magnifications of the carbon paper without (Fig. 3a and c), with electrodeposited MoS_2 (Fig. 3b and d), and with MoS_2 modified with PIM-1 nanoparticles (Fig. 3e and f). The carbon paper is a highly porous three-dimensional network of carbon fibers each having a diameter of about 10 μm. The surface of the bare carbon fiber is impregnated with Teflon film. Fig. 3b shows the image of the carbon paper with electrodeposited MoS_2, where a uniform MoS_2 film covers all the carbon paper. Fig. 3d reveals the spherical form of the MoS_2 nuclei in a film. According to the literature,[22,34–36] this type of morphology is typical for amorphous MoS_2 films. The weight of MoS_2 produced under these conditions (50 deposition cycles) was typically 0.3 mg. Further deposition did not improve performance. For PIM-$1_{(120\ \mu g)}$/MoS_2/CP, Fig. 3f reveals aggregated PIM-1 nanoparticles with typically 50–100 nm diameter deposited over the MoS_2 film.

Fig. 4a shows the XRD pattern for MoS_2/CP and PIM-$1_{(120\ \mu g)}$/MoS_2/CP catalysts. The diffraction peaks at 26.5, 42.4, 44.6, 54.6 and 77.4° corresponds to (002), (100), (101), (004) and (110) planes of the hexagonal structure of graphite (PDF no. 00-041-1487) from the carbon paper substrate. In contrast, no peaks for MoS_2 were observed. The absence of characteristic diffraction peaks indicates MoS_2 is amorphous. These

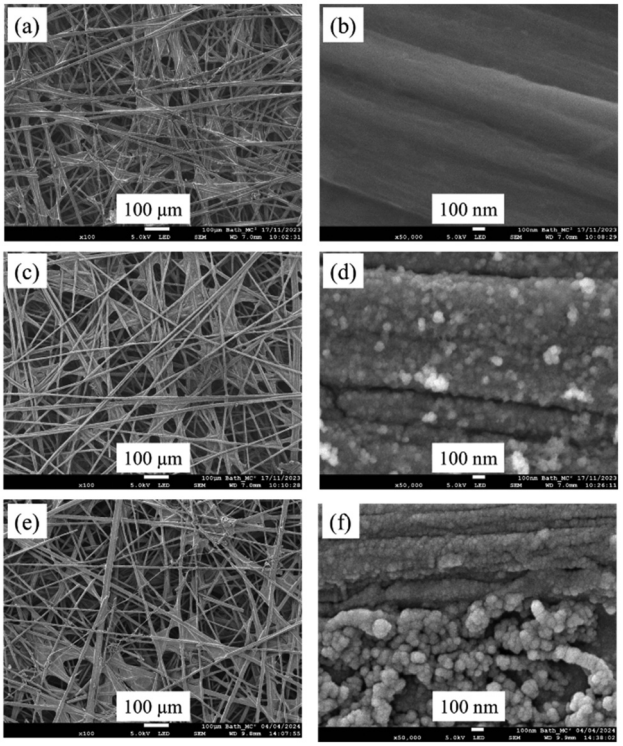

Fig. 3 SEM images at different magnifications for bare carbon paper (a) 100×, (b) 50k×, MoS_2/CP (c) 100×, (d) 50k× and PIM-$1_{(120\ \mu g)}$/MoS_2/CP (e) 100× and (f) 50k×.

findings are consistent with reports in the literature for electrodeposited MoS_x films.[34,36]

To further confirm the amorphous nature of the as-prepared catalysts, Raman scattering spectra are recorded and shown in Fig. 4b. All spectra presented the D (1380 cm^{-1}) and G bands (1572 cm^{-1}) that are related to, respectively, the vibration of carbon atoms in disordered regions and the stretching of the C–C bond and the in-plane hexagonal vibrations of C–C in a graphitic structure.[37]

In addition, the spectra obtained for MoS_2/CP and PIM-$1_{(120\ \mu g)}$/MoS_2/CP catalysts resemble those of amorphous MoS_2 films.[21,35,36] Despite their amorphous nature, the films presented the $E_{2g}^{(1)}$ (375–388 cm^{-1}) and A_{1g} (400–415 cm^{-1}) modes ascribed to the in-plane Mo–S and the out-plane Mo–S vibrational modes of MoS_2, respectively.[38–40] Raman peaks from 530 to 545 cm^{-1} are assigned to $(S–S)_{terminal}$ and $(S–S)_{bridging}$ vibrations in disulfide ligands, respectively.[38,41]

The Raman active modes between 800–1100 cm^{-1} are assigned to terminal oxygen atoms in the MoS_2 film, indicating the presence of MoO_3 on both MoS_2 catalysts.[42,43] This is due to the oxidation of the material in the region of laser irradiation since the experiment was conducted in atmospheric conditions.[44] The oxidation of MoS_2 during the synthesis could occur, since OH^- is produced during cathodic deposition (eqn (1)).[44] In mono-layered MoS_2 the distance between $E_{2g}^{(1)}$ and A_{1g} is approximately 18 cm^{-1} and this distance increases with thickness.[41,43] The frequency difference

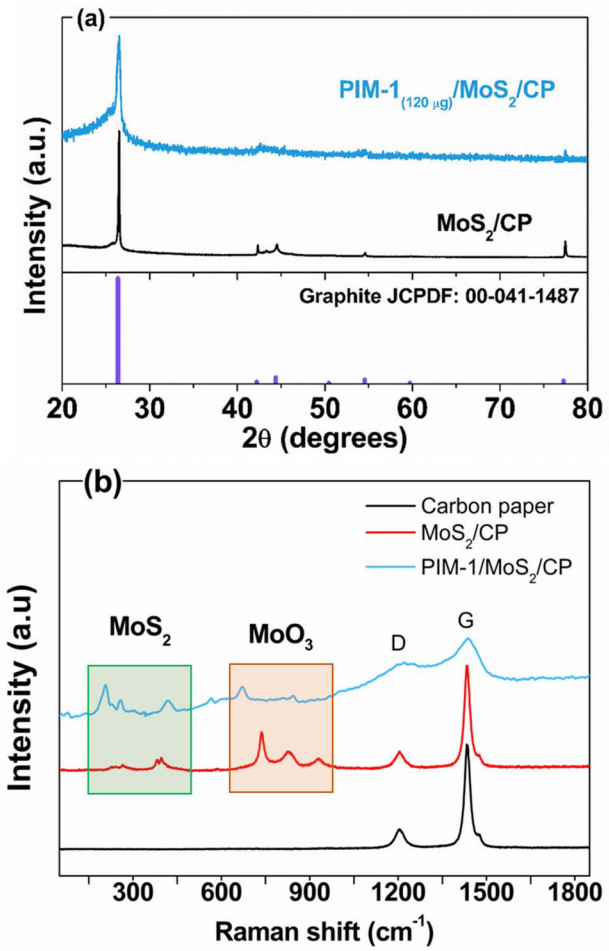

Fig. 4 (a) XRD patterns for MoS_2/CP and PIM-$1_{(120\ \mu g)}$/MoS_2/CP catalysts. (b) Raman spectra (532 nm) recorded on carbon paper, MoS_2/CP and PIM-$1_{(120\ \mu g)}$/MoS_2/CP materials.

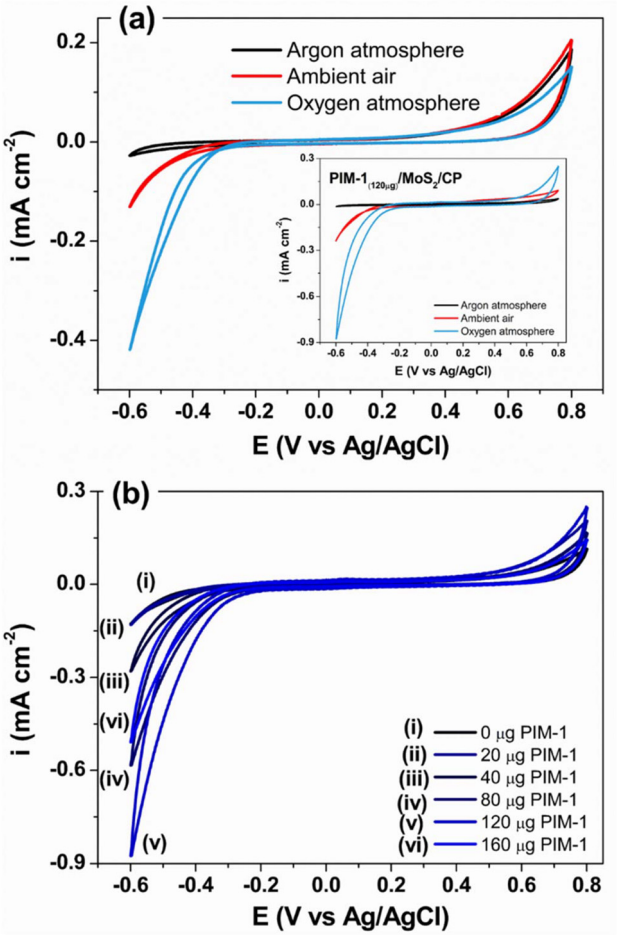

Fig. 5 (a) Cyclic voltammograms (scan rate 50 mV s^{-1}) for MoS_2/CP and PIM-$1_{(120\ \mu g)}$/MoS_2 (inset) in 0.1 mol L^{-1} phosphate buffer pH 7 for different gas environments. (b) Cyclic voltammograms (scan rate 50 mV s^{-1}) in ambient air for MoS_2/CP with different amounts of PIM-1 nanoparticles deposits (20–160 μg).

of 27 cm^{-1} between the two fundamental modes confirms the bulk character of the synthesized films.

Effects of nanoparticulate PIM-1 on dioxygen reduction catalysis

The electrochemical reduction of oxygen on MoS_2 is investigated as a test system for gas phase reduction. Fig. 5a shows cyclic voltammograms (scan rate 50 mV s^{-1}) for MoS_2/CP and PIM-$1_{(120\ \mu g)}$/MoS_2 (inset) in 0.1 mol L^{-1} phosphate buffer pH 7 in different gas environments. The absence of a peak associated with oxygen reduction suggests that oxygen reduction and hydrogen evolution reactions may occur simultaneously catalyzed by the active sites of MoS_2. In ambient air or oxygen-purged solution, there is an increase in current, indicative of oxygen reduction. To rule out the influence of carbon support on oxygen reduction, cyclic voltammograms were obtained on bare carbon in different gas environments (Fig. S3a†). As shown in the voltammograms with the electrolyte saturated with O_2 (Fig. S3b†), the currents for the carbon support are negligible compared to those observed with MoS_2/CP and PIM-1/MoS_2/CP catalysts.

Next, different amounts of PIM-1 nanoparticles (20–160 μg) were deposited on MoS_2/CP (Fig. 5b). For the MoS_2/CP (0 μg PIM-1) in ambient air a cathodic current of −129 μA cm^{-2} is achieved. The cathodic current is significantly improved in the presence of varying amounts of PIM-1 nanoparticles on the MoS_2/CP. With 120 μg of PIM-1 nanoparticles, the current is three times higher. Such an increase in current can be associated either with fast diffusion or, more likely, an enhanced concentration/activity of oxygen locally at the electrode surface in the presence of the PIM-1 nanoparticles.[28,30,45]

To further demonstrate the ability of PIM-1 nanoparticles to store/release oxygen gas, chronoamperometric tests (Fig. 6a) were performed in O_2-saturated 0.1 mol L^{-1} phosphate buffer solution (PBS, pH 7) and the production of H_2O_2 was monitored quantitatively by mass spectrometry (using *p*-nitrophenyl boronic acid, see experimental in ESI†).

According to Fig. 6b, the production of H_2O_2 remains constant and the yield increases during the reaction time. However, the presence of PIM-1 nanoparticle deposit signifi-

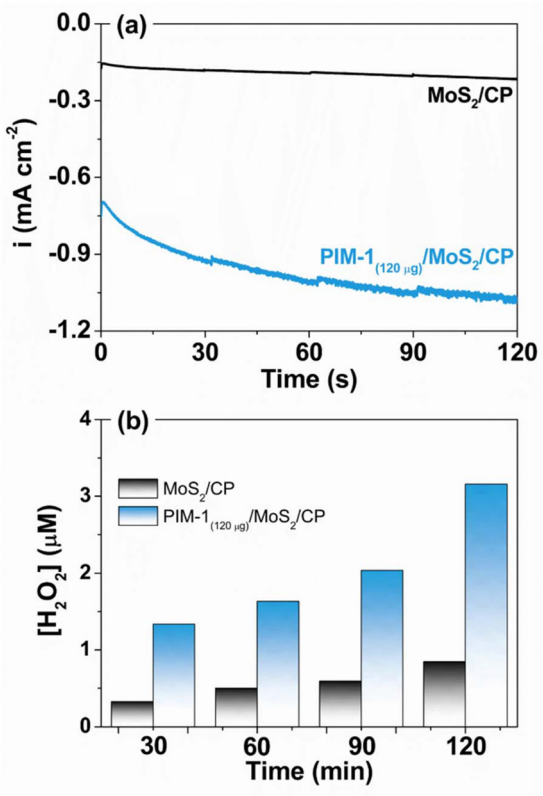

Fig. 6 (a) Chronoamperometry data (with stirring, volume 60 mL) in O_2-saturated 0.1 mol L^{-1} PBS (pH 7) solution at −0.6 V *vs.* Ag/AgCl and (b) time profiles of H_2O_2 production for MoS_2/CP and PIM-$1_{(120\ \mu g)}$/MoS_2/CP catalysts.

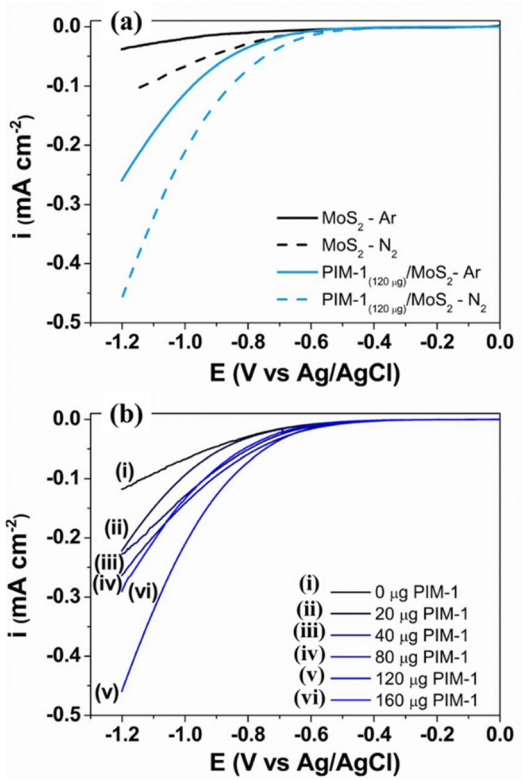

Fig. 7 (a) Linear sweep voltammograms (scan rate of 5 mV s^{-1}) for MoS_2/CP and for PIM-$1_{(120\ \mu g)}$/MoS_2/CP in 0.1 mol L^{-1} PBS (pH 7) electrolyte saturated with N_2 and Ar. (b) Linear sweep voltammograms for MoS_2/CP with different amounts of PIM-1 nanoparticles deposits (20–160 μg) in 0.1 mol L^{-1} PBS (pH 7) electrolyte saturated with N_2.

cantly increases the H_2O_2 production, reaching a value of 3.16 μM after 2 h of reaction, almost 4 times higher than that for MoS_2/CP catalyst alone (0.85 μM). These results corroborate that oxygen is stored/accumulated in the nanoparticulated PIM-1 deposits and released in a kinetically controlled reaction, leading to an apparently higher concentration/activity and additional H_2O_2 production. The same principle can be applied to the nitrogen reduction reaction, as demonstrated below.

Effects of nanoparticulate PIM-1 on nitrogen reduction catalysis

Linear sweep voltammetry is employed to evaluate the nitrogen reduction reactivity for MoS_2/CP and for PIM-1/MoS_2/CP catalysts. As shown in Fig. 7a, the voltammetric curves reveal an onset potential for nitrogen reduction around −0.6 V *vs.* Ag/AgCl. With the increase in the overpotential, an increase in reduction current can be observed in the N_2-saturated solution (as compared to Ar-saturated electrolyte), indicating that both catalysts are active for nitrogen reduction. To limit the competition from hydrogen evolution, the potential window for the nitrogen reduction experiments is selected in the range from −0.6 V to −1.0 V *vs.* Ag/AgCl.

Fig. 7b shows voltammograms obtained in N_2-saturated electrolytes with different amounts of PIM-1 nanoparticle deposits (20–160 μg) on MoS_2/CP. The presence of PIM-1 nanoparticles substantially increases the cathodic current, reaching a value 3-fold higher for PIM-$1_{(120\ \mu g)}$/MoS_2/CP catalyst than for MoS_2/CP. This significant current increase may indicate more nitrogen reacting on the electrode surface. However, there is a slight drop in current values when 160 μg of PIM-1 is deposited on MoS_2 possibly due to an increase in the resistivity impeding the overall process. All further experiments are performed with 120 μg PIM-1.

The impact of depositing PIM-1 nanoparticles on nitrogen reduction on the MoS_2/CP catalyst was assessed further by performing chronoamperometric tests, followed by LC-MS measurements to quantify ammonia production. Fig. S2 and S4† show the standard calibration curves for estimating NH_3 and N_2H_4 concentrations, respectively. PIM-$1_{(120\ \mu g)}$/MoS_2/CP catalyst was employed in electrolysis at different potentials for 2 h (Fig. 8a). The NH_3 yield rates and faradaic efficiency were obtained (Fig. 8b). As shown in Fig. 8c, there is an increase in the NH_3 yield rate and faradaic efficiency when the applied potential is more negative. The highest NH_3 yield of 61.2 μg h^{-1} mg^{-1} and faradaic efficiency of 45.4% are achieved at −0.85 V *vs.* Ag/AgCl, exceeding most reported Mo-based electrocatalyst performances (Table S1†). However, when the potential is more negative than −0.85 V *vs.* Ag/AgCl, the nitro-

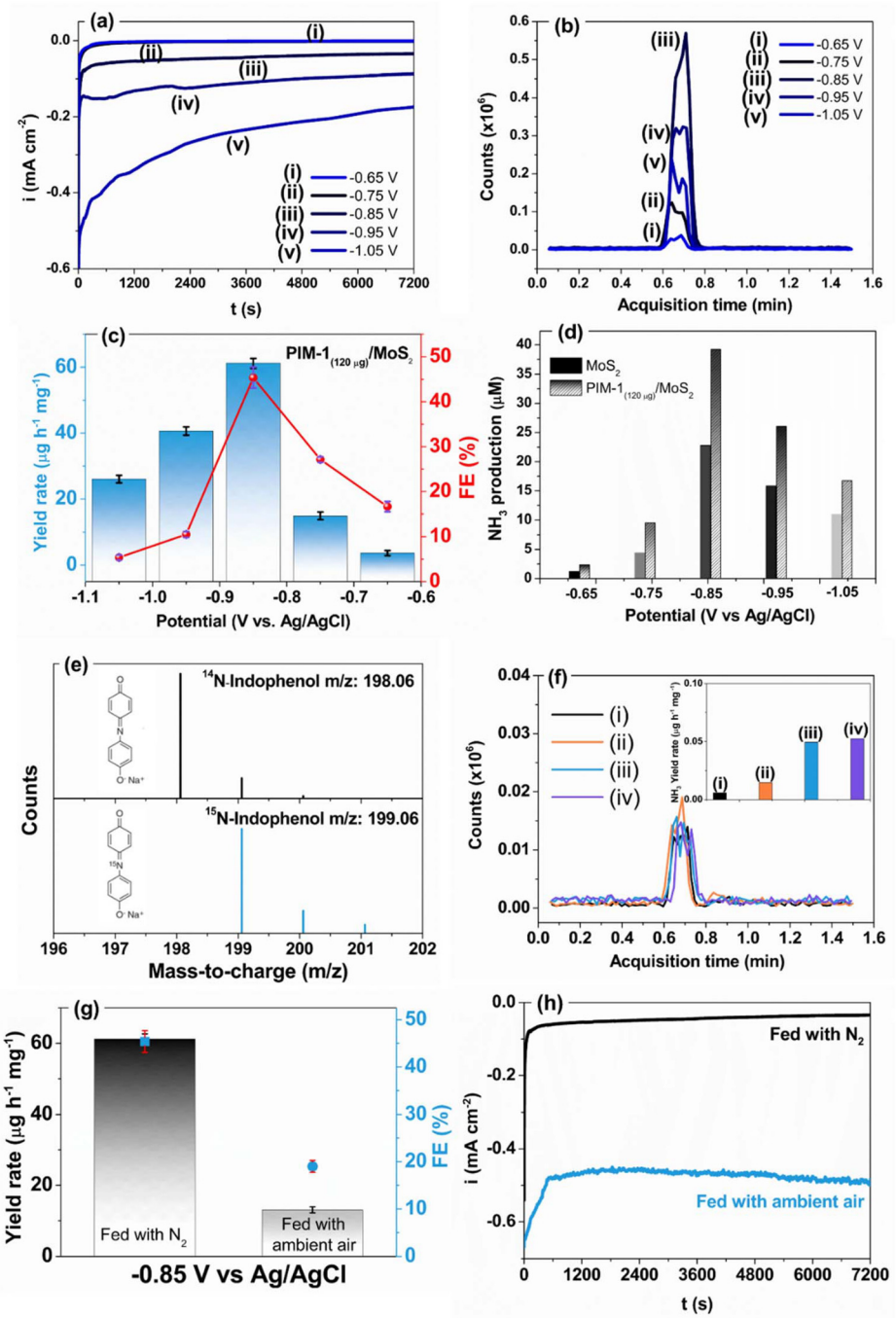

Fig. 8 (a) Chronoamperometry electrolysis (2 h) at various potentials for PIM-1$_{(120\ \mu g)}$/MoS_2/CP, (b) corresponding counts *versus* acquisition time for LC-MS data for indophenol indicator from ammonia produced at different potentials. (c) NH_3 yield rate and faradaic efficiency (FE) values for PIM-1$_{(120\ \mu g)}$/MoS_2/CP. (d) NH_3 production comparison between MoS_2/CP and PIM-1$_{(120\ \mu g)}$/MoS_2/CP at different potentials. (e) The mass spectrum for electrolyte samples collected after isotope labelling nitrogen reduction experiments by PIM-1$_{(120\ \mu g)}$/MoS_2/CP catalyst demonstrating formation of ^{14}N-indophenol and ^{15}N-indophenol, respectively. (f) LC chromatogram peak integration for indophenol and MS mass signal for 2 h electrolysis (i) under argon, (ii) without current flow under argon, (iii) without current flow under nitrogen, and (iv) using bare carbon paper electrodes. In all cases, the ammonia detection remains negligible. (g) Comparison of NH_3 yield rate and faradaic efficiency values for PIM-1$_{(120\ \mu g)}$/MoS_2/CP in N_2-saturated and air-saturated solution. (h) Chronoamperometry electrolysis (2 h) at −0.85 V *vs.* Ag/AgCl in N_2-saturated (black curve) and air-saturated (blue curve) solution for PIM-1$_{(120\ \mu g)}$/MoS_2/CP.

gen reduction activity of PIM-1$_{(120\ \mu g)}$/MoS_2/CP decreases, especially for the faradaic efficiency, where a considerable decay is observed. This decay is attributed here to the enhanced/competing hydrogen evolution at higher overpotentials.[46–48] The byproduct N_2H_4 remains undetectable (Fig. S4c†), demonstrating a high nitrogen reduction selectivity of PIM-1$_{(120\ \mu g)}$/MoS_2/CP.

To achieve further insight into the effect of PIM-1 nanoparticle deposition on the nitrogen reduction activity of MoS_2, the nitrogen reduction performance of MoS_2/CP is considered (Fig. S5†). MoS_2/CP showed a lower nitrogen reduction performance than PIM-1$_{(120\ \mu g)}$/MoS_2/CP, reaching an NH_3 yield rate of 35.6 μg h^{-1} mg^{-1}, almost a factor two lower than that for PIM-1$_{(120\ \mu g)}$/MoS_2/CP, with a faradaic efficiency of 38%. As presented in Fig. 8d, the catalyst modified with PIM-1 nanoparticles outperformed the MoS_2/CP NH_3 production at all considered potentials. Such improvement indicates a higher concentration/activity of N_2 locally at the electrode surface in the presence of gas trapped in the PIM-1 nanoparticles.[28,49]

To verify the origin of the nitrogen source, isotopic labelling measurements were carried out with gaseous $^{15}N_2$ (≥98 atom % ^{15}N, Cambridge Isotope Laboratories, Inc.; Fig. 8e). Similar investigations in the past have been based on NMR evidence,[50–52] but here the LC-MS detection tool is employed to verify isotopic labelling. After conducting electrolysis with a PIM-1$_{(120\ \mu g)}$/MoS_2/CP electrode using either $^{15}N_2$ or $^{14}N_2$ as feed gas, LC-MS is used to distinguish between ammonia isotopologues ($^{15}NH_3$ and $^{14}NH_3$) due to their distinct mass-to-charge (*m*/*z*) values for ^{14}N-indophenol (*m*/*z*: 198) and for ^{15}N-indophenol (*m*/*z*: 199). The production of ammonia ($^{15}NH_3$ and $^{14}NH_3$) using either $^{15}N_2$ or $^{14}N_2$ as feed gas are similar, as described in Fig. S6.† When using Ar as the feed gas, only traces of indophenol are detected (Fig. 8f). This confirms that NH_3 is most likely produced here from gaseous nitrogen in the electrochemical nitrogen reduction process.[49]

Next, the selectivity by the PIM-1$_{(120\ \mu g)}$/MoS_2/CP catalyst for N_2 or O_2 reduction reaction was evaluated by feeding the electrolyte with ambient air (30 mL min^{-1}) with the aid of a peristaltic pump. The air contains around 78% V/V nitrogen. Therefore, it presents an attractive source of molecular nitrogen that can be used for ammonia electrosynthesis, although oxygen reduction is expected to interfere. When the electrolyte was fed with ambient air, there was a drop in the values of NH_3 production rate and in faradaic efficiency of the reaction, as shown in Fig. 8g. This decrease indicates competition between N_2 and O_2 reduction for binding into the active sites of the catalyst. The NH_3 yield rates were lower compared to those in N_2-saturated electrolyte. The higher reduction current density (Fig. 8h) in the air-saturated solution is attributed to the contribution of the oxygen reduction. However, the NH_3 yield rates and faradaic efficiency (13 μg h^{-1} mg^{-1} and 19.0%, respectively) with the air-saturated electrolyte are still comparable to the performance of many catalysts reported in the literature for pure nitrogen atmosphere (see Table S1†). Therefore, the hypothesis that air can be used as a substitute for pure nitrogen is confirmed. Fig. S7† shows that effects from ammonia introduced by air feed remain insignificant. However, further optimization as well as consideration of NO_x impurities in air as potential contributors to ammonia production will be required in the future work.

To evaluate the nitrogen reduction catalyst durability of PIM-1$_{(120\ \mu g)}$/MoS_2/CP, long-term operation (20 h) electrolysis and six chronoamperometric repeat experiments are performed. After six chronoamperometric experiments (Fig. 9a), only minor fluctuations were observed for the corresponding NH_3 yield rates and faradaic efficiencies (Fig. 9b) and for the counts *versus* acquisition time measurements (Fig. S8†). This confirmed the good cycling stability of the material. The current remained stable for over 20 h of continuous electrolysis (Fig. 9c), indicating that PIM-1$_{(120\ \mu g)}$/MoS_2/CP is durable after an initial decrease in the first few minutes of the

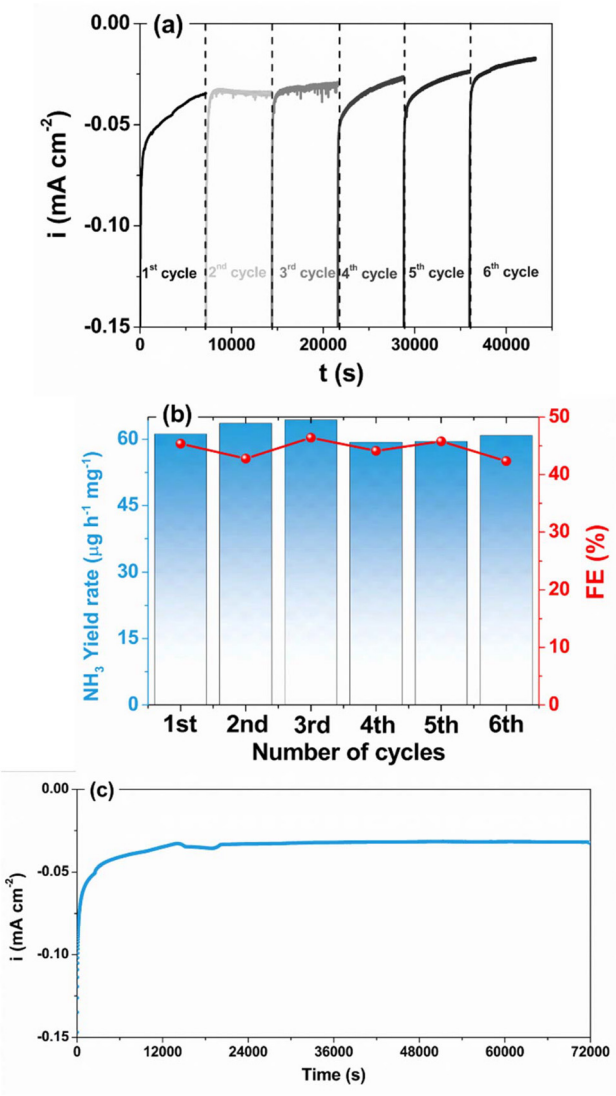

Fig. 9 (a) Chronoamperometry data for PIM-1$_{(120\ \mu g)}$/MoS_2/CP for six cycles and (b) corresponding NH_3 yield rates and faradaic efficiencies (FE). (c) Chronoamperometry data for PIM-1$_{(120\ \mu g)}$/MoS_2/CP for 20 h of nitrogen reduction electrolysis at −0.85 V *vs.* Ag/AgCl.

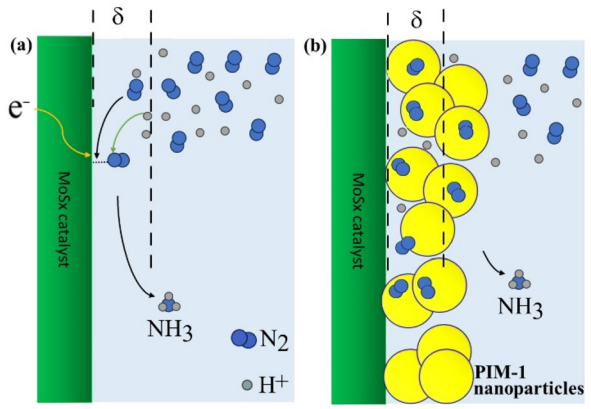

Fig. 10 Illustration of (a) N_2 reduction at the catalyst|electrolyte interface, (b) with PIM-1 nanoparticles acting as N_2 reservoir. To be effective, the additional N_2 supply must be within d, the diffusion or reaction layer.

measurement. This durability can be attributed to mild conditions and the mechanical strength of the material, as evidenced by the well-preserved morphology observed after the stability test (Fig. S9a–S9c†).

Mechanistic effects of nanoparticulate PIM-1 on triphasic O_2 or N_2 electroreduction

The effect of PIM-1 nanoparticles on triphasic N_2 reduction is shown schematically in Fig. 10. For nitrogen reduction, both NH_3 yield rates and faradaic efficiencies increase in the presence of PIM-1 nanoparticles (Fig. 10b), indicating a locally higher apparent N_2 concentration under triphasic conditions (*i.e.* trapped nanobubbles). The supply of N_2 (or O_2 for oxygen reduction) has to be within the diffusion or reaction layer at the electrode surface (for diffusion or kinetically controlled processes, respectively). Plausible here seems a physical trapping of nitrogen (or oxygen) gas within the hydrophobic PIM-1 micropores. Nanoscale gas inclusions can contain gas at higher pressure due to surface tension effects. The observed increase in nitrogen reduction rate is linked to a locally increased apparent concentration and activity of reactants.

Conclusion

Interfacial engineering can be employed to locally enhance apparent concentration and activity of gaseous species close to electrode surfaces. Without changing the catalytic site, the catalytic environment can be designed to improve performance. Here, the performance of amorphous MoS_2 catalyst for the electrochemical reduction of N_2 under ambient conditions is shown to improve by depositing a film of PIM-1 nanoparticles over the MoS_2 catalyst. We found that depositing 120 μg of PIM-1 nanoparticles effectively increased both the activity and selectivity of MoS_2, resulting in an NH_3 yield rate of 61.2 μg h^{-1} mg^{-1}, almost twice higher than bare MoS_2/CP (35.6 μg h^{-1} mg^{-1}). The faradaic efficiency was as high as 45.4% at −0.85 V *vs.* Ag/AgCl in 0.1 M PBS at pH 7, which is competitive when compared to nitrogen reduction studies using gas diffusion electrodes and Ru catalysts.[53] The mechanism behind these improvements is proposed to be related to the ability of PIM-1 to store gaseous N_2 close to the catalyst surface in a triphasic reaction environment. The enhanced local activity of nitrogen (similar to using increased pressure) affects the kinetically controlled electroreduction. Essentially, with the effect of PIM-1 nanoparticles (or similar gas binding materials) on the apparent gas solubility, it is now possible to work with an engineered electrode surface and avoiding the need for a gas diffusion electrode.

Although very high efficiency in nitrogen fixation has been reported in non-aqueous media,[54] the use of direct air feed in aqueous buffer media is desirable. Oxygen reduction would be expected to dominate, but kinetic control in the process reported here allows ammonia to be obtained, although at lowered efficiency. In the context of ammonia production by electroreduction, the problem of impurities for example in the gas feed has been raised.[50,55] Electrocatalytic reduction requires mass transport to the interface and is thereby less sensitive to trace impurities when compared to biological nitrogen fixation, but effects due to the presence for example of NO_x in the gas feed especially when using air feed cannot be ruled out. Although electrocatalysis on amorphous MoS_2 seems relatively uncontroversial, the work with direct air feed will require further confirmation, for example by performing experiments with $^{15}NO_x$ tracer, or under pressure and without air flow.

This work offers an efficient catalyst interface for catalytic synthesis of NH_3, and it provides a simple PIM-1 nanoparticle deposition strategy that can be extended to the design of other high-performance catalyst interfaces for N_2 reduction (or for other types of gas-consuming reactions under triphasic conditions). In the future, the molecular structure of the PIM and the loading and electrode morphology can be further improved to enhance catalyst performance by surface engineering for a wider arrange of processes.

Author contributions

Caio V. S. Almeida: investigation, data curation and formal analysis, writing – original draft – review & editing; Lara K. Ribeirio: investigation, data curation and formal analysis, writing – review & editing; Lucia H. Mascaro: supervision writing – review & editing; Mariolino Carta: resources, writing – review & editing; Neil B. McKeown: resources, supervision, writing – review & editing; Frank Marken: supervision, writing – review & editing.

Data availability

The data supporting this article have been included as part of the ESI.†

Conflicts of interest

There are no conflicts to declare.

Acknowledgements

L. H. M. thanks FAPESP (2013/07296-2; #2017/11986-5), CNPq (#405133/2023-5, #311769/2022-5) and FINEP (#01.22.0179.00, #01.23.0645.00) and Shell and the strategic importance of the support given by ANP (Brazil's National Oil, Natural Gas and Biofuels Agency) through the R&D levy regulation. C. V. S. A. thanks FAPESP (2021/14693-4, 2023/07295-8). L. K. R. thanks CNPq for support (200978/2024-1). F. M. thanks the Leverhulme Trust and EPSRC for support (EP/K004956/1).

References

1 B. Yang, W. Ding, H. Zhang and S. Zhang, *Energy Environ. Sci.*, 2021, **14**, 672.
2 J. G. Chen, R. M. Crooks, L. C. Seefeldt, K. L. Bren, R. M. Bullock, M. Y. Darensbourg, P. L. Holland, B. Hoffman, M. J. Janik, A. K. Jones, M. G. Kanatzidis, P. King, K. M. Lancaster, S. V. Lymar, P. Pfromm, W. F. Schneider and R. R. Schrock, *Science*, 2018, **360**, eaar6611.
3 J. W. Erisman, M. A. Sutton, J. Galloway, Z. Klimont and W. Winiwarter, *Nat. Geosci.*, 2008, **1**, 636.
4 T. Wu, W. Fan, Y. Zhang and F. Zhang, *Mater. Today Phys.*, 2021, **16**, 100310.
5 L. Wang, M. Xia, H. Wang, K. Huang, C. Qian, C. T. Maravelias and G. A. Ozin, *Joule*, 2018, **2**, 1055.
6 F. Liu, A. R. Fernie and Y. J. Zhang, *Trends Plant Sci.*, 2024, **29**, 1168.
7 T. H. Coale, V. Loconte, K. A. Turk-Kubo, B. Vanslembrouck, W. K. E. Mak, S. Cheung, A. Ekman, J. H. Chen, K. Hagino and Y. Takano, *Science*, 2024, **384**, 217.
8 K. Jayakumar, D. Sakthilatha and R. Venkatesan, *ChemistrySelect*, 2025, **10**, e202500224.
9 S. L. Foster, S. I. P. Bakovic, R. D. Duda, S. Maheshwari, R. D. Milton, S. D. Minteer, M. J. Janik, J. N. Renner and L. F. Greenlee, *Nat. Catal.*, 2018, **1**, 490.
10 T. Zibert, B. Likozar and M. Hus, *ChemSusChem*, 2024, **17**, 01730.
11 S. S. Zheng, F. Y. Zhang, Y. M. Jiang, T. Xu, H. Li, H. Guo and Y. Zhou, *Front. Chem. Sci. Eng.*, 2024, **18**, 112.
12 X. H. Wang, B. Wu, Y. F. Zhu, D. S. Wang, N. B. Li, Z. I. Xu and H. Q. Luo, *Nano-Micro Lett.*, 2025, **17**, 182.
13 W. R. Zhao, J. Zhang, X. Zhu, M. Zhang, J. Tang, M. Tan and Y. Wang, *Appl. Catal., B*, 2014, **144**, 468.
14 P. Li, Z. Liu, T. Wu, Y. Zhang, L. Wang, L. Wang, L. Ji, Y. Zhang, Y. Luo, T. Wang, S. Liu, Y. Wu, M. Liu and X. Sun, *J. Mater. Chem. A*, 2019, **7**, 17761.
15 S. Chen, X. Liu, J. Xiong, L. Mi and Y. Li, *Mater. Today Nano*, 2022, **18**, 100202.
16 J. Mukherjee, A. Adalder, N. Mukherjee and U. K. Ghorai, *Catal. Today*, 2023, **423**, 113905.
17 X. Liu, Y. Jiao, Y. Zheng, M. Jaroniec and S. Z. Qiao, *J. Am. Chem. Soc.*, 2019, **141**, 9664.
18 C. Lv, C. Yan, G. Chen, Y. Ding, J. Sun, Y. Zhou and G. Yu, *Angew. Chem., Int. Ed.*, 2018, **57**, 6073.
19 C. Lv, L. Zhong, Y. Yao, D. Liu, Y. Kong, X. Jin, Z. Fang, W. Xu, C. Yan, K. N. Dinh, M. Shao, L. Song, G. Chen, S. Li, Q. Yan and G. Yu, *Chem*, 2020, **6**, 2690.
20 B. Vedhanarayanan, C.-C. Chiu, J. Regner, Z. Sofer, K. C. Seetha Lakshmi, J.-Y. Lin and T.-W. Lin, *Chem. Eng. J.*, 2022, **430**, 132649.
21 L. Tian, J. X. Zhao, X. Ren, X. Sun, Q. Wei and D. Wu, *ChemistryOpen*, 2021, **10**, 1041.
22 C. V. S. Almeida and L. H. Mascaro, *Electrochim. Acta*, 2024, **476**, 143680.
23 S. Chen, X. Liu, J. Xiong, L. Mi and Y. Li, *Mater. Today Nano*, 2022, **18**, 100202.
24 M. Arif, M. Babar, U. Azhar, M. Sagir, M. B. Tahir, M. A. Mushtaq, G. Yasin, M. Mubashir, J. W. R. Chong, K. S. Khoo and P. L. Show, *J. Chem. Eng.*, 2023, **451**, 138320.
25 X. Chen, C. Ma, Z. Tan, X. Wang, X. Qian, X. Zhang, J. Tian, S. Yan and M. Shao, *Chem. Eng. J.*, 2022, **433**, 134504.
26 Y. Zhao, N. A. Al Abass, R. Malpass-Evans, M. Carta, N. B. McKeown, E. Madrid, P. J. Fletcher and F. Marken, *Electrochem. Commun.*, 2019, **103**, 1.
27 Y. Wang, B. S. Ghanem, Z. Ali, K. Hazazi, Y. Han and I. Pinnau, *Small Struct.*, 2021, **2**, 2100049.
28 E. Madrid, J. P. Lowe, K. J. Msayib, N. B. McKeown, Q. L. Song, G. A. Attard, T. Düren and F. Marken, *ChemElectroChem*, 2019, **6**, 252.
29 A. Mahajan, S. K. Bhattacharya, S. Rochat, A. D. Burrows, P. J. Fletcher, Y. Y. Rong, A. B. Dalton, N. B. McKeown and F. Marken, *ChemElectroChem*, 2019, **6**, 4307.
30 M. Azevedo Beluomini, N. Ramos Stradiotto, M. V. Boldrin Zanoni, M. Carta, N. B. McKeown, P. J. Fletcher, S. Sain, Z. K. Li and F. Marken, *ACS Appl. Mater. Interfaces*, 2024, **16**, 37865.
31 S. C. Perry, S. M. Gateman, R. Malpass-Evans, N. McKeown, M. Wegener, P. Nazarovs, J. Mauzeroll, L. Wang and C. Ponce de Leon, *Chemosphere*, 2020, **248**, 125993.
32 C. G. Morales-Guio and X. L. Hu, *Acc. Chem. Res.*, 2014, **47**, 2671.
33 J. Tan, W. Yang, Y. Oh, H. Lee, J. Park and J. Moon, *ACS Appl. Mater. Interfaces*, 2018, **10**, 10898.
34 S. C. Lee, J. D. Benck, C. Tsai, J. Park, A. L. Koh, F. Abild-Pedersen, T. F. Jaramillo and R. Sinclair, *ACS Nano*, 2016, **10**, 624.
35 H. Sun, X. Ji, Y. Qiu, Y. Zhang, Z. Ma, G.-G. Gao and P. Hu, *J. Alloys Compd.*, 2019, **777**, 514.
36 O. Mabayoje, Y. Liu, M. Wang, A. Shoola, A. M. Ebrahim, A. I. Frenkel and C. B. Mullins, *ACS Appl. Mater. Interfaces*, 2019, **11**, 32879.
37 A. J. Mendoza, M. A. Hickner, J. Morgan, K. Rutter and C. Legzdins, *Fuel Cells*, 2011, **11**, 248.
38 Y. Deng, L. R. L. Ting, P. H. L. Neo, Y.-J. Zhang, A. A. Peterson and B. S. Yeo, *ACS Catal.*, 2016, **6**, 7790.
39 C. G. Morales-Guio and X. Hu, *Acc. Chem. Res.*, 2014, **47**, 2671.

40 G. Papadimitropoulos, N. Vourdas, A. Kontos, M. Vasilopoulou, D. N. Kouvatsos, N. Boukos, A. Gasparotto, D. Barreca and D. Davazoglou, *Phys. Status Solidi C*, 2015, **12**, 969.
41 T. Daeneke, N. Dahr, P. Atkin, R. M. Clark, C. J. Harrison, R. Brkljaca, N. Pillai, B. Y. Zhang, A. Zavabeti, S. J. Ippolito, K. J. Berean, J. Z. Ou, M. S. Strano and K. Kalantar-zadeh, *ACS Nano*, 2017, **11**, 6782.
42 R. Murugan, A. Ghule, C. Bhongale and H. J. Chang, *J. Mater. Chem.*, 2000, **10**, 2157.
43 B. Susmitha, K. Arjun and B. Karthikeyan, *Appl. Phys. A*, 2023, **129**, 309.
44 H. Vrubel and X. Hu, *ACS Catal.*, 2013, **3**, 2002.
45 Y. Zhao, N. A. Al Abass, R. Malpass-Evans, M. Carta, N. B. McKeown, E. Madrid, P. J. Fletcher and F. Marken, *Electrochem. Commun.*, 2019, **103**, 1.
46 J. Wang, H. Nan, Y. Tian and K. Chu, *ACS Sustainable Chem. Eng.*, 2020, **8**, 12733.
47 S. Murmu, S. Paul, A. Santra, M. Robert and U. K. Ghorai, *Catal. Today*, 2023, **423**, 113938.
48 G. Peng, J.-W. Zhao, J. Wang, E. Hoenig, S. Wu, M. Wang, M. He, L. Zhang, J.-X. Liu and C. Liu, *Appl. Catal., B*, 2023, **338**, 123020.
49 J. B. Spinelli, L. P. Kelley and M. C. Haigis, *Sci. Rep.*, 2017, **7**, 10304.
50 S. Z. Andersen, V. Čolić, S. Yang, J. A. Schwalbe, A. C. Nielander, J. M. McEnaney, K. Enemark-Rasmussen, J. G. Baker, A. R. Singh, B. A. Rohr, M. J. Statt, S. J. Blair, S. Mezzavilla, J. Kibsgaard, P. C. K. Vesborg, M. Cargnello, S. F. Bent, T. F. Jaramillo, I. E. L. Stephens, J. K. Nørskov and I. Chorkendorff, *Nature*, 2019, **570**, 504.
51 R. Y. Hodgetts, A. S. Kiryutin, P. Nichols, H.-L. Du, J. M. Bakker, D. R. Macfarlane and A. N. Simonov, *ACS Energy Lett.*, 2020, **5**, 736.
52 J. Choi, B. H. R. Suryanto, D. Wang, H.-L. Du, R. Y. Hodgetts, F. M. Ferrero Vallana, D. R. MacFarlane and A. N. Simonov, *Nat. Commun.*, 2020, **11**, 5546.
53 X. Wei, M. H. Pu, Y. M. Jin and M. Wessling, *ACS Appl. Mater. Interfaces*, 2021, **13**, 21411.
54 H.-L. Du, M. Chatti, R. Y. Hodgetts, P. V. Cherepanov, C. K. Nguyen, K. Matuszek, D. R. MacFarlane and A. N. Simonov, *Nature*, 2022, **609**, 722.
55 R. Dabundo, M. F. Lehmann, L. Treibergs, C. R. Tobias, M. A. Altabet, P. H. Moisander and J. Granger, *PLoS One*, 2014, **9**, e110335.